



OPEN ACCESS

EDITED BY
Peng Li,
Tianjin University, China

REVIEWED BY
Narottam Das,
Central Queensland University, Australia
Mahidur Sarker,
National University of Malaysia, Malaysia

*CORRESPONDENCE
Yuanhao Ye,
1055051305@qq.com

SPECIALTY SECTION
This article was submitted to Smart
Grids, a section of
the journal Frontiers in
Energy Research

RECEIVED 29 July 2022
ACCEPTED 31 October 2022
PUBLISHED 13 January 2023

CITATION
Liu G, Ye Y, Luo B, Gu Y, Zheng W and
Chen S (2023), Structural optimization
and simulation of piezoelectric-
piezoresistive coupled MEMS steady-
state electric field sensor.
Front. Energy Res. 10:1006777.
doi: 10.3389/fenrg.2022.1006777

COPYRIGHT
© 2023 Liu, Ye, Luo, Gu, Zheng and
Chen. This is an open-access article
distributed under the terms of the
[Creative Commons Attribution License
\(CC BY\)](https://creativecommons.org/licenses/by/4.0/). The use, distribution or
reproduction in other forums is
permitted, provided the original
author(s) and the copyright owner(s) are
credited and that the original
publication in this journal is cited, in
accordance with accepted academic
practice. No use, distribution or
reproduction is permitted which does
not comply with these terms.

Structural optimization and simulation of piezoelectric-piezoresistive coupled MEMS steady-state electric field sensor

Guote Liu¹, Yuanhao Ye^{1*}, Bing Luo², Yu Gu³, Weijia Zheng¹ and Sijun Chen⁴

¹School of Mechatronic Engineering and Automation, Foshan University, Foshan, China, ²China Southern Power Grid Technology Research Institute Co., Ltd, Guangzhou, China, ³China Southern Power Grid Co. Ltd EHV Transmission Company Guangzhou Bureau, Guangzhou, China, ⁴Guangdong Shuangdian Technology Co., Ltd, Dongguan, China

Abstract: In view of the problems of large volume, high energy consumption and difficult maintenance of electric field measurement sensors in existing power systems, non-contact miniature electric field sensors have become a hot topic in current research. In this paper, a MEMS miniature electric field measurement sensor model based on the principle of piezoelectric-piezoresistive coupling is constructed, and the sensor structure is optimized by analyzing the steady-state characteristics of the piezoelectric material and semiconductor membrane of the sensor. The input and output characteristics of the sensor were tested. The test results show that the sensor has excellent mechanical strain capacity, and the output voltage of the sensor has a linear relationship with the electric field strength, thus verifying the feasibility of the sensor measurement in the electric field. The research results will provide some reference for the development of contactless coupled sensors.

KEYWORDS

electric field measurement, MEMS sensor, finite element simulation, piezoelectric effect, piezoresistive effect

1 Introduction

Electric field measurement technology is indispensable in the field of the power system. Typical electric field measurement applications in the field of electrical engineering include DC electric field in the valve hall of the converter station (Wang et al., 2015; Zhang et al., 2019), measurement of the power frequency electric field on the surface of the insulator (Liu et al., 2018; Liu et al., 2019), etc. Accurately measuring the electric field changes in the space around the power equipment is of great significance to the design, manufacture, and safe operation of the power equipment. The emergence of the integrated electric field sensor is a major development in electric field measurement. The electric field sensor is a non-invasive voltage measurement device for the primary system. At present, the

measurement of electric field is mainly using field-mill sensors (Cui et al., 2017; Yong et al., 2018) and optical electric field sensors, field-mill sensors induce the charge generated in the electric field, and these induced charges are periodically changed in the rotational shielding electrode to obtain a current of induced charge. It is generally used for the measurement of ground-level electromagnetic environment, and the stability is poor in strong electric field environment. Optical electric field sensors mainly include electric field sensors based on the Pockels effect (Zeng et al., 2013; Yang et al., 2015; Aristizabal-Tique et al., 2020) and the Kerr effect (Wu et al., 2012; Qi et al., 2016), which are highly priced and the sensitivity is greatly affected by frequency.

Micro Electro Mechanical Systems (MEMS) is a new type of electromechanical device formed from the processing of traditional semiconductor microelectronic devices. Compared with the above sensors, MEMS sensors have the advantages of small size, lightweight and low cost. Ideal for electric field measurement sensors. MEMS sensors have significant application effects in the fields of temperature detection (Ando et al., 2011; Frantlovic et al., 2016), pressure measurement (Nag et al., 2020; Sahay and Jindal, 2021), and humidity detection (Chen et al., 2016; Zhao et al., 2021), and are gradually becoming the development direction and research focus of electric field sensors. At present, the miniature electric field sensor based on MEMS technology is mainly based on the resonant structure of the charge sensing principle (KAINZ et al., 2018; Shanhong et al., 2021), All induction designs have shield plates moving above the induction electrode and shielding electrode by moving laterally. For example, literature (TORUNBALCI et al., 2015) adopts a vertically moving shutter structure. In the literature (IQBAL and LEE, 2018), the shield plate and the electrode are on the same plane, and the moving shield plate changes its shielding of the edge electric field around the electrode. Unlike conventional sensors, electric field sensing based on the coupling mechanism is an indirect measurement of the conversion of electric field energy into other energy that can be directly measured. Compared with the direct electric field induction measurement, the device size of the interface coupled sensing method can be reduced to the order of millimeters or even microns, which reduces the requirements for the insulation and electromagnetic interference resistance of the test circuit and has high stability.

Therefore, this paper uses the finite element method to build a MEMS micro electric field measurement sensor model based on piezoelectric-piezoresistive coupled, the first part introduces the basic structure and working principle of the sensor. The second part studies the steady-state characteristics of electric field sensors under piezoelectric materials and semiconductor membranes of different sizes, and selects the key parameters of the sensor structure. The third part tests the output characteristics of the sensor in a uniform electric field, thus verifying the feasibility of the sensor in electric field measurement.

2 Sensor test principle

The sensor is mainly composed of two parts coupled with piezoelectric material and piezoresistive material. Due to the inverse piezoelectric effect, the dimensional changes in the thickness, length, and width of the piezoelectric material in the electric field will drive the piezoresistive material to deform. Through the piezoresistive effect, the resistance value of the varistor on the piezoresistive material changes, and finally the electric field can be effectively measured by the electrical signal output by the piezo resistor. The internal structure and appearance of the sensor are shown in Figure 1 and Figure 2.

The sensor coupling system is composed of a piezoelectric-mechanical system and a piezoresistive system. The piezoelectric-mechanical system is in the electric field and mechanical strain. The inverse piezoelectric effect can be expressed as a matrix.

$$\begin{bmatrix} X_1 \\ X_2 \\ X_3 \\ X_4 \\ X_5 \\ X_6 \end{bmatrix} = \begin{bmatrix} d_{11} & d_{21} & d_{31} \\ d_{12} & d_{22} & d_{32} \\ d_{13} & d_{23} & d_{33} \\ d_{14} & d_{24} & d_{34} \\ d_{15} & d_{25} & d_{35} \\ d_{16} & d_{26} & d_{36} \end{bmatrix} \begin{bmatrix} E_1 \\ E_2 \\ E_3 \end{bmatrix} \tag{1}$$

where x is the strain, d is the piezoelectric constant matrix, and E is the applied electric field strength matrix.

$$\begin{aligned} X_1 &= S_{11}^E X_1 + d_{31} E_3 \\ D_3 &= d_{31} x_1 + \epsilon_{33}^x E_3 \end{aligned} \tag{2}$$

where x_1 is the strain tensor, X_1 is the stress tensor, S is the short-circuit elastic compliance constant, d_{31} is the free dielectric constant, and d_{31} is the voltage constant.

Changes in varistor resistance are caused by strain-induced changes in the material's band structure and associated changes in carrier mobility and number density. The relationship between the electric field E and the current I in the varistor is:

$$E = \rho \cdot I + \Delta \rho \cdot I \tag{3}$$

where ρ is the resistivity and $\Delta \rho$ is the induced change in resistivity. In the general case, both ρ and $\Delta \rho$ are rank two tensors. The resistance change is related to the stress X , and the constitutive relationship between the two is:

$$\Delta \rho = \Pi \cdot X \tag{4}$$

where Π is the varistor tensor, which is a material property. If resistivity and stress are converted to vectors using simplified subscript notation, then it can be represented as a matrix.

$$\begin{bmatrix} \Delta \rho_{xx} \\ \Delta \rho_{yy} \\ \Delta \rho_{zz} \\ \Delta \rho_{yz} \\ \Delta \rho_{xz} \\ \Delta \rho_{xy} \end{bmatrix} = \begin{bmatrix} \Pi_{11} & \Pi_{12} & \Pi_{13} & \Pi_{14} & \Pi_{15} & \Pi_{16} \\ \Pi_{21} & \Pi_{22} & \Pi_{23} & \Pi_{24} & \Pi_{25} & \Pi_{26} \\ \Pi_{31} & \Pi_{32} & \Pi_{33} & \Pi_{34} & \Pi_{35} & \Pi_{36} \\ \Pi_{41} & \Pi_{42} & \Pi_{43} & \Pi_{44} & \Pi_{45} & \Pi_{46} \\ \Pi_{51} & \Pi_{52} & \Pi_{53} & \Pi_{54} & \Pi_{55} & \Pi_{56} \\ \Pi_{61} & \Pi_{62} & \Pi_{63} & \Pi_{64} & \Pi_{65} & \Pi_{66} \end{bmatrix} \cdot \begin{bmatrix} X_{xx} \\ X_{yy} \\ X_{zz} \\ X_{yz} \\ X_{xz} \\ X_{xy} \end{bmatrix} \tag{5}$$

The relationship between the internal electric field and current can also be expressed by a matrix as:

$$\begin{bmatrix} E_X \\ E_Y \\ E_Z \end{bmatrix} = \begin{bmatrix} \rho_{xx} & \rho_{xy} & \rho_{xz} \\ \rho_{xy} & \rho_{yy} & \rho_{yz} \\ \rho_{xz} & \rho_{yz} & \rho_{zz} \end{bmatrix} \cdot \begin{bmatrix} I_x \\ I_y \\ I_z \end{bmatrix} + \begin{bmatrix} \Delta\rho_{xx} & \Delta\rho_{xy} & \Delta\rho_{xz} \\ \Delta\rho_{xy} & \Delta\rho_{yy} & \Delta\rho_{yz} \\ \Delta\rho_{xz} & \Delta\rho_{yz} & \Delta\rho_{zz} \end{bmatrix} \cdot \begin{bmatrix} I_x \\ I_y \\ I_z \end{bmatrix} \quad (6)$$

There is shear stress in a varistor, which is a result of the stress of the piezoelectric material in the semiconductor membrane. Through the piezoresistive effect, these shear stresses create an electric field or potential gradient in the varistor bridge arms transverse to the direction of the current flow. In the entire width of the varistor, the potential gradients are added together to generate an induced voltage difference between different bridge arms, and the electric field strength can be inferred from the magnitude of the generated voltage.

3 Finite element model design

3.1 Sensor benchmark model

Based on the process theory of MEMS micro-sensors, the structure of the piezoelectric-piezoresistive coupled electric field measurement sensor is optimized. To obtain the optimal size of the sensor, the model design needs to meet:

- 1)The deformation of the piezoelectric material in the electric field is maximized;
- 2)The piezoresistive membrane can vibrate freely on the device;
- 3)The piezoelectric material is firmly coupled with the piezoresistive material.

Based on the above points, the conventional sensor parameters were selected, a sensor model with semiconductor membranes edge length of 500 μm, a thickness of 20 μm, piezoelectric material edge length of 350 μm and thickness of 300 μm is established.

The side length of the membrane is larger than the side length of the piezoelectric material so that the surrounding of the membrane is highly coupled with the glass and plays a fixed role. The glass layer has air pockets that provide enough space for the membrane to vibrate. The piezoelectric material is the same height as the glass, embedded in the glass layer, and the pyramid glass fixes the piezoelectric material. The substrate is made of glass, and is reliably fixed with the lower surface of the piezoelectric crystal so that the crystal is deformed along the positive direction of the z-axis, the strain is transmitted to the semiconductor membrane to the maximum extent, and the measurement accuracy of the sensor is improved. The X-Z planar structure of the sensor is shown in Figure 3.

The sensor material parameters are shown in Table 1.

The model sets the substrate, glass, and piezoelectric material as fixed constraints to ensure that the piezoelectric material

TABLE 1 Material settings of each part of the sensor.

Piezoelectric material	Semiconductor membrane	Base
Zinc Oxide	Si-Silicon	SiO2

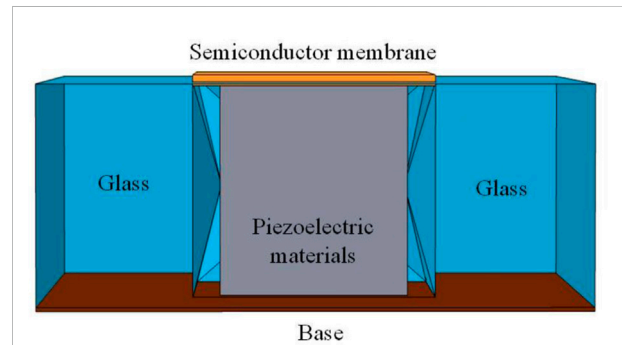


FIGURE 1 Schematic diagram of the sensor interior.

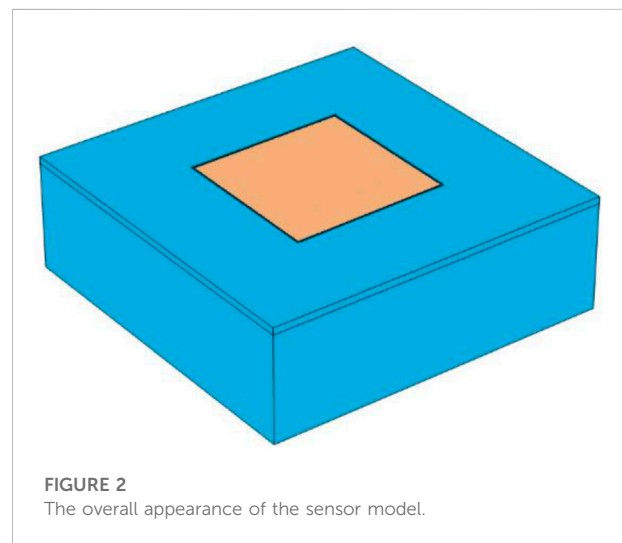
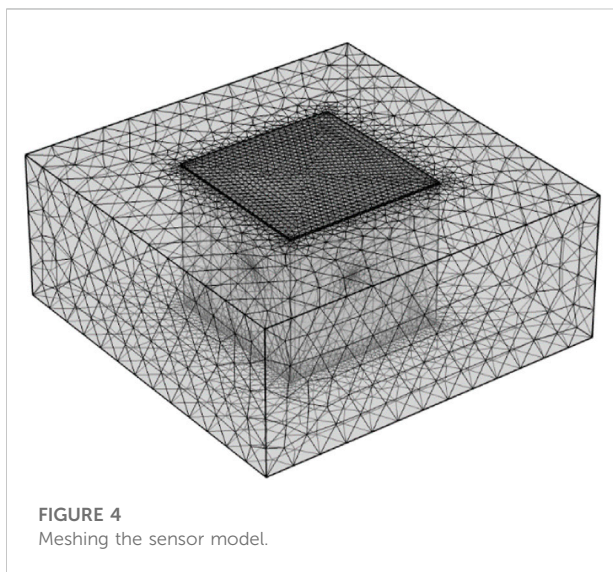
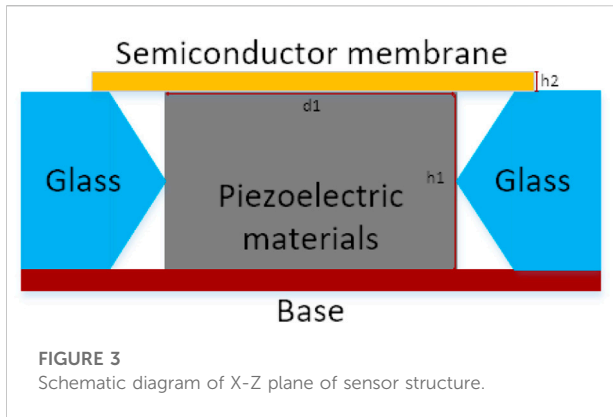


FIGURE 2 The overall appearance of the sensor model.

deforms only in the positive direction of the z-axis. The ground terminal is the lower surface of the piezoelectric material, the voltage terminal is the upper surface of the piezoelectric material, and the voltage value is 1000 V.

3.2 Meshing

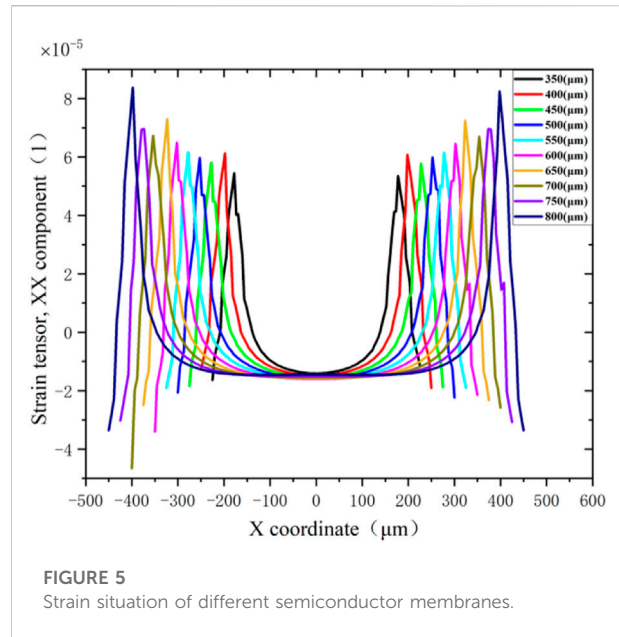
The finite element method (FEM) was introduced by Comsol Multiphysics software to optimize the sensor structure.



To improve the calculation accuracy and calculation speed, the research objects are divided into piezoelectric materials, semiconductor membranes, glass, and substrates. The calculation grid is divided by free tetrahedrons. Since the main objects of size optimization are piezoelectric materials and semiconductor membranes, Therefore, more detailed mesh division is performed on piezoelectric materials and semiconductor membranes, as shown in Figure 4.

3.3 Structural size selection

The main optimization work of the sensor model is the optimization of semiconductor membrane and piezoelectric material. By using the method of control variable, the influence of the edge length and thickness of semiconductor membrane and piezoelectric material on the sensor performance



is gradually explored to select the optimal parameters and complete the optimization of the sensor structure.

3.3.1 Piezoelectric material side length

The side length of the piezoelectric material is studied by parametric scanning, starting from the side length of the piezoelectric material $d_1 = 350 \mu\text{m}$, with a step size of $50 \mu\text{m}$, and ending at $d_1 = 800 \mu\text{m}$, the steady state study is carried out, the strain and displacement of piezoelectric materials with different side lengths in the steady electric field are obtained.

Analysis of Figure 5 and Figure 6 shows that the strain component and displacement increase from the center of the membrane at $X = 0$, reach a peak near the boundary of the piezoelectric material, and then decrease. The displacement peaks of piezoelectric materials with different side lengths differ slightly, but the strains vary greatly. In the material with side length less than $550 \mu\text{m}$, the strain peak of $400 \mu\text{m}$ side length is the highest, which is 6×10^{-5} . Compared with the membrane with side length of $600 \mu\text{m}$ – $800 \mu\text{m}$, the strain is reduced by 15%–20%, but the side length is reduced. The piezoelectric material with a side length of $400 \mu\text{m}$ is selected to reduce the volume of the sensor based on ensuring the sensitivity of the sensor, and the strain performance is better, and it is also conducive to the miniaturization of the sensor design.

3.3.2 Piezoelectric material thickness

Keep the side length of the piezoelectric material at $400 \mu\text{m}$, and change the thickness h_1 of the piezoelectric material block to conduct steady-state research, starting from $h_1 = 200 \mu\text{m}$, with a step size of $50 \mu\text{m}$, and ending at $h_1 = 1000 \mu\text{m}$. The strain and

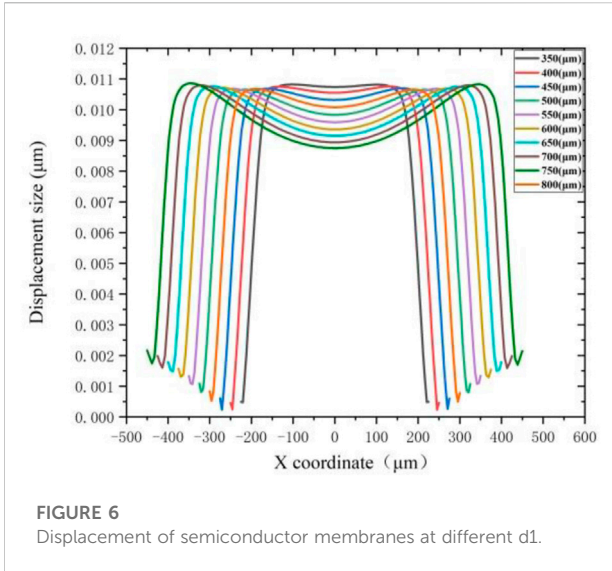


FIGURE 6 Displacement of semiconductor membranes at different d_1 .

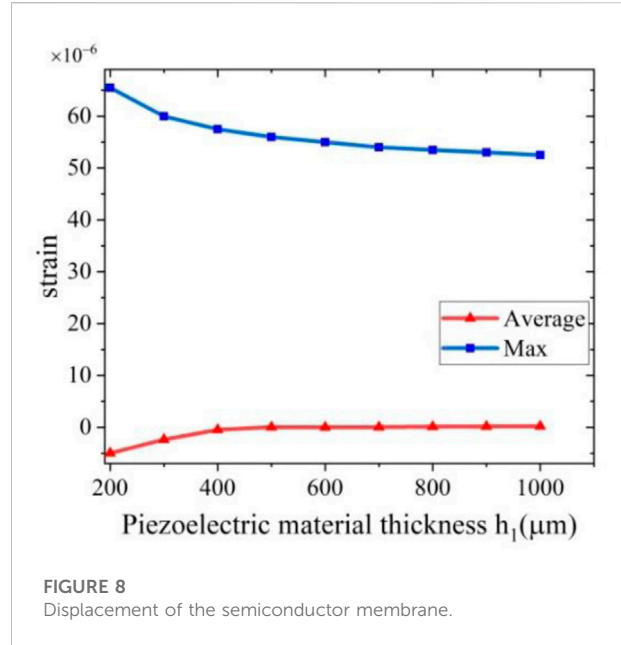


FIGURE 8 Displacement of the semiconductor membrane.

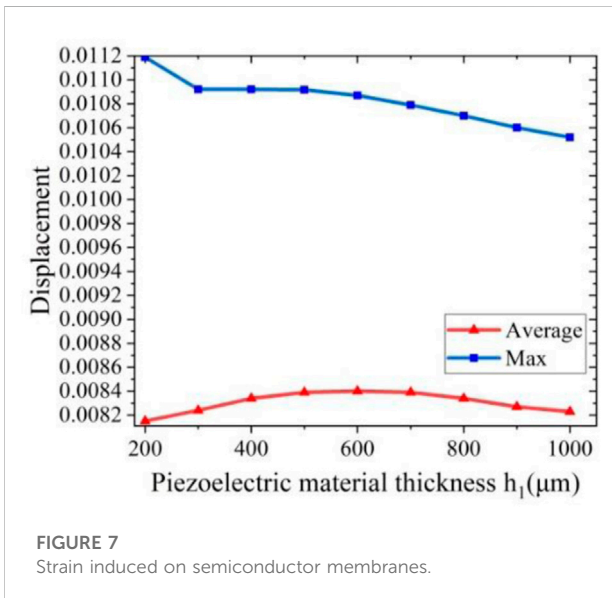


FIGURE 7 Strain induced on semiconductor membranes.

deformation results of piezoelectric materials with different thicknesses in steady electric field are obtained.

Analysis of Figure 7 and Figure 8 shows that as the thickness of the piezoelectric material increases, the piezoelectric effect becomes more obvious, the overall strain increases, but the distance between the cavities becomes shorter and the strain peak decreases. Therefore, both the strain amount and the maximum deformation displacement on the semiconductor membrane show a downward trend; the average strain amount increases first and then tends to be stable, and the displacement amount first increases and then decreases slowly. The piezoelectric thickness in the range of $300 \leq h_1 \leq 400$ material, the strain component is kept at a high 60×10^{-6} , which is better than other piezoelectric materials.

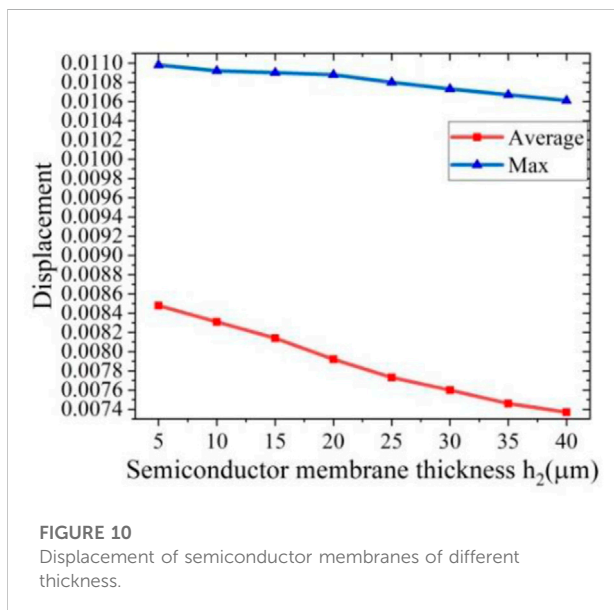
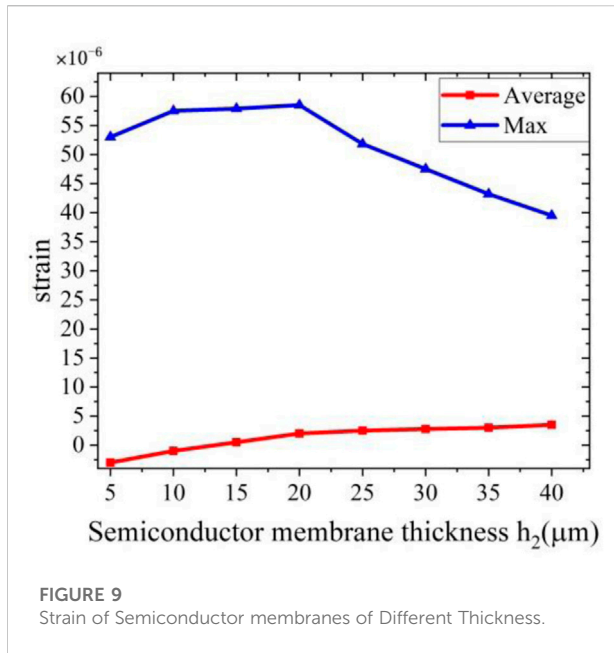
Considering the optimal strain and displacement factors, the piezoelectric material with thickness $h_1 = 350 \mu\text{m}$ is the best.

3.3.3 Semiconductor membrane thickness

Keep the side length of the piezoelectric material as $d_1 = 400$, the thickness of the piezoelectric material $h_1 = 350 \mu\text{m}$, change the thickness h_2 of the semiconductor membrane, start from $h_2 = 5 \mu\text{m}$, step $5 \mu\text{m}$, and stop at $h_2 = 40 \mu\text{m}$, carry out steady-state research, and obtain different thicknesses strain and deformation results of semiconductor thin-membrane devices in steady-state electric fields.

Analysis of Figure 9 and Figure 10 shows that as the thickness of the semiconductor membrane increases, its strain sensitivity decreases, the maximum strain on the membrane first increases slowly and then decreases, the average value increases slowly, and the displacement decreases. When the membrane thickness is less than $15 \mu\text{m}$, the average value of the strain is negative. Therefore, when analyzing the semiconductor membrane with a thickness of $20 \mu\text{m}$ – $40 \mu\text{m}$, the maximum displacement and strain decrease with the increase of the membrane thickness, and the maximum strain peak of the $20 \mu\text{m}$ membrane is $60 \mu\text{m} \times 10^{-6}$, the smaller the thickness, the more obvious the strain, therefore, the semiconductor membrane with thickness $h_2 = 20 \mu\text{m}$ is the best.

Based on the above results and combined with semiconductor membrane side length of the initial model, the piezoelectric material with side length $d_1 = 400 \mu\text{m}$, thickness $h_1 = 350 \mu\text{m}$, and semiconductor membrane with thickness $h_2 = 20 \mu\text{m}$ and side length $d_2 = 500 \mu\text{m}$ are used as the benchmark model to ensure the sensitivity of the sensor, and consider the design and processing, etc. Factors to meet the optimization needs of electric field measurement sensors.



4 Electric field measurement sensor performance simulation

After obtaining the optimized structural parameters of the sensor, the steady-state response simulation of the sensor structure is carried out on this model to test the performance of the sensor.

4.1 Selection of doping regions in semiconductor membranes

By analyzing the strain distribution of the sensor on the surface of the semiconductor membrane under the electric field of 1000V, it is obtained that the strain component σ_{XX} along the X axis is almost the same as the strain component σ_{YY} along the Y axis, so only σ_{XX} will be studied in the future, As shown in Figure 11.

According to previous research, the boundary between the semiconductor membrane and the piezoelectric material is the region with the largest strain, which is the optimal design position of the doped region. Since the strain distribution gradient near the boundary is large, and the positive and negative strains appear alternately, the selection of the appropriate ion doping region has a great impact on the sensor performance.

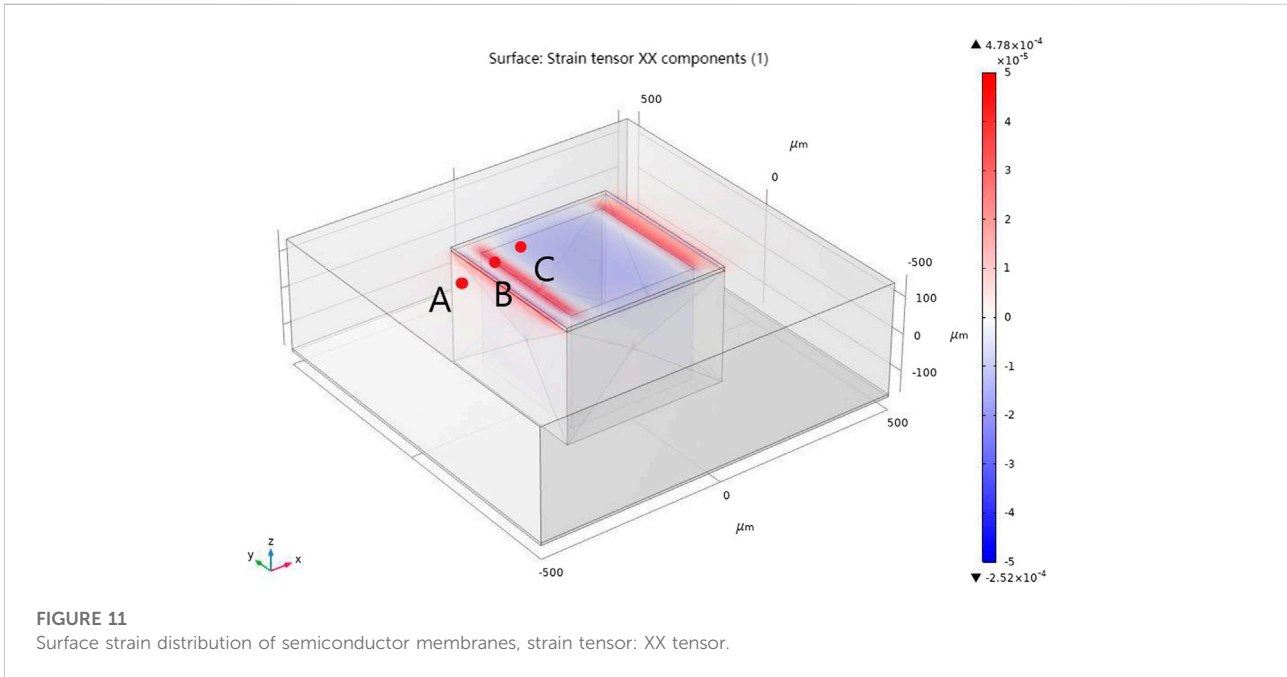
Through analysis, point A (-230, 0, 150), B (-220, 0, 150), and C (-210, 0, 150) are all located in the area with large boundary strain. Analysis of Figure 11 shows that points B and C are in the positive and negative strain change regions, and the sensitivity is low. Therefore, point A is studied. Figure 12A shows the strain tensor σ_{XX} of the membrane along the x-axis, and Figure 12B shows the strain tensor σ_{XX} of the membrane along the y-axis. Two regions A and B are taken in Figure 11, corresponding to the regions A and B in Figure 12, and the point A' is the zero point of the strain tensor σ_{XX} at A and B.

A_x is obtained by integrating the strain tensor in the yellow part of Figure 12A and the area enclosed by $\sigma_{XX} = 0$, and A_y is obtained by integrating the strain tensor in the yellow area in Figure 12B and the area enclosed by $\sigma_{XX} = 0$, where A_x and A_y are doping area strain tensor. The strain tensors in the blue area are processed in the same way to obtain B_x and B_y as the strain tensors of the B area. B_y comparing the integral area, the strain tensor at A is significantly larger than that at B. Therefore, in a comprehensive analysis, the position of A is the best area for ion doping.

4.2 Design of piezoresistive patch

After the semiconductor doping area is determined, a piezo resistor patch is placed on the thin membrane of the above-mentioned benchmark model, so that the model has a bridge structure for outputting electrical signals, as shown in the gray part of Figure 13.

Set the X bridge of the varistor at the place where the semiconductor membrane has the greatest strain. As shown in Figure 14, set a 3 V voltage on the upper left arm of the X bridge, and connect the lower right arm to the ground. In the electric



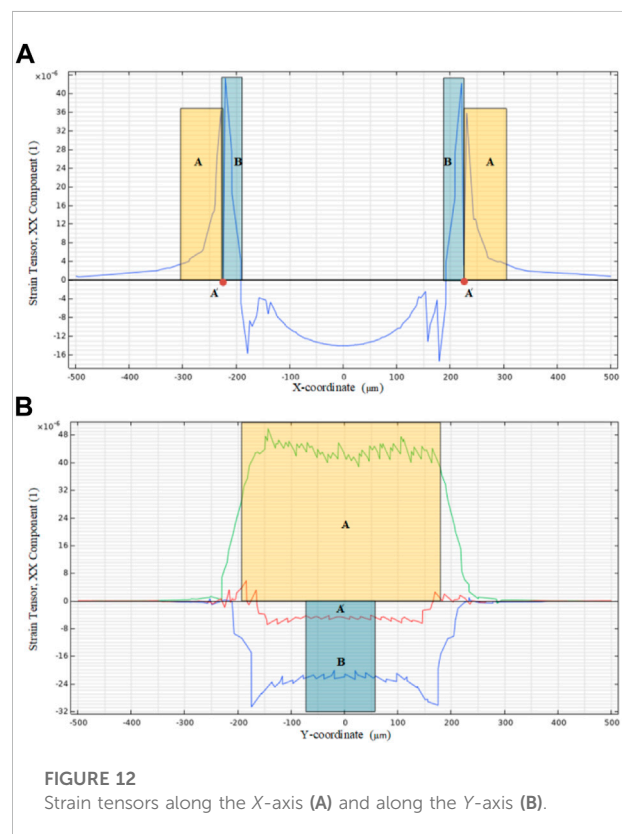
field, the piezoelectric material induces deformation, which drives the semiconductor membrane to apply shear stress on the varistor, making the potential distribution uneven, and the bridge arm will generate an induced voltage difference, as shown in Figure 15.

When testing the performance indicators of the electric field sensor, it needs to be carried out in a quantifiable uniform electric field environment. Test methods and platforms for traditional electric field sensors are usually based on a uniform electric field formed by standard parallel metal plates. According to the principle of parallel plate electric field: ideally, a stable voltage of different amplitudes can be loaded on two parallel plate electrodes of infinite size and a certain distance, and a uniform electric field can be formed between the parallel plates, and the electric field direction is perpendicular to the two parallel plates, and the electric field strength can be calculated from Equation 7.

$$E = \frac{U}{d} \tag{7}$$

Here, E is the electric field strength of the sensor; U is the difference in DC voltage applied across the sensor; d is the sensor height. The electric field sensor is placed in the middle of the parallel plate electric field device, the voltage applied to both ends of the sensor is changed, the electric field strength E is generated, and the output amount of the electric field sensor is recorded, so that the relationship between the input electric field strength E and U_{out} can be determined, and the input and output characteristics of the electric field sensor can be obtained.

In Table 2, V₁ is the voltage applied to the upper end of the piezoelectric material. In the range of 0 V ~ -1000V, the electric field strength is 0–2.86 × 10⁻⁶V/m.



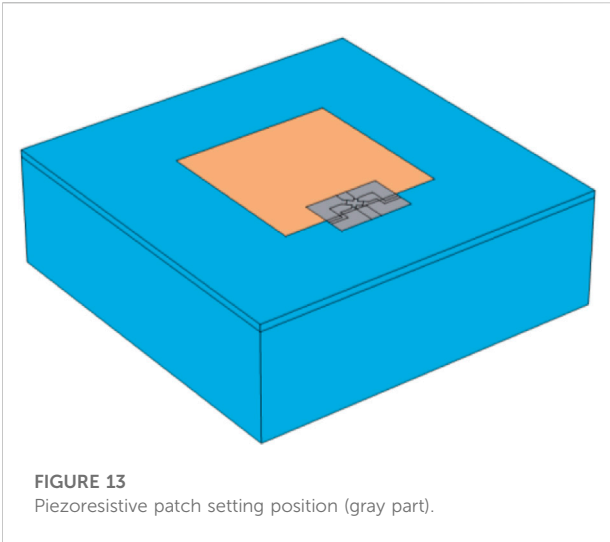


FIGURE 13
Piezoresistive patch setting position (gray part).

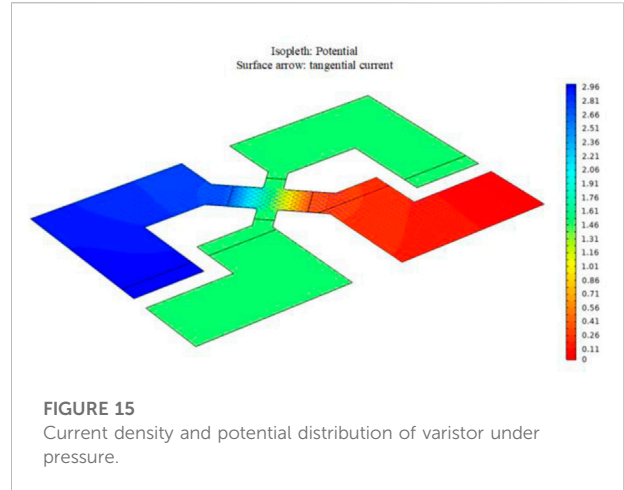


FIGURE 15
Current density and potential distribution of varistor under pressure.

TABLE 2 Working current and output voltage of varistor driven by 3 V applied voltage.

V_1	Device output(V)
0.0000	0.00003077
100.00	0.00006611
200.00	0.00010143
300.00	0.00013672
400.00	0.00017199
500.00	0.00020723
600.00	0.00024245
700.00	0.00027765
800.00	0.00031282
900.00	0.00034797
1,000.0	0.0003831

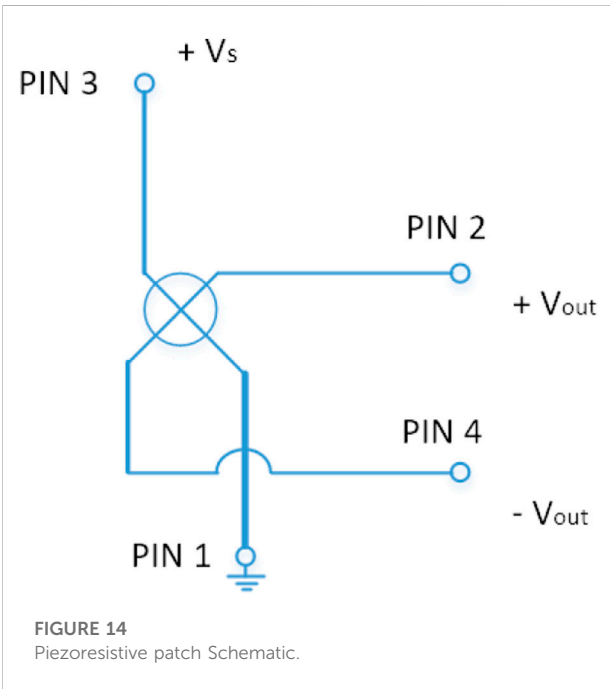


FIGURE 14
Piezoresistive patch Schematic.

Analysis of Figure 16 shows that the electric field where the piezoelectric material is located is different, and the voltage value output by the patch is also different. The output voltage of the patch has a linear relationship with the applied voltage of the piezoelectric material. Therefore, the electric field intensity of the sensor can be obtained by the voltage signal output from the piezoresistive patch.

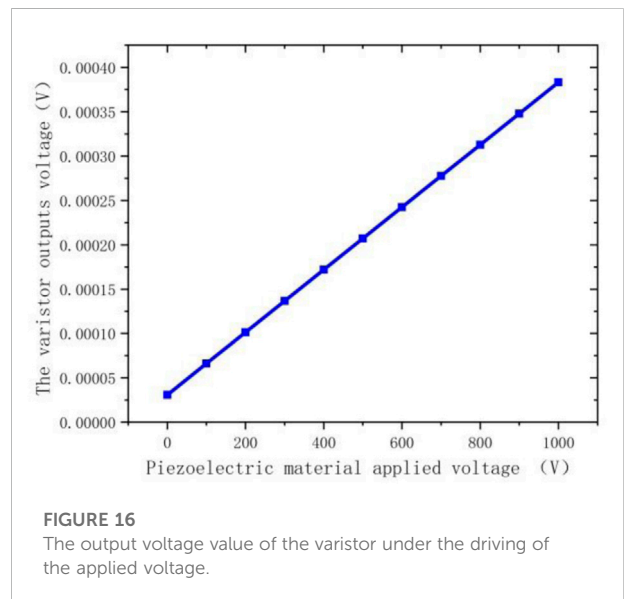


FIGURE 16
The output voltage of the varistor under the driving of the applied voltage.

5 Conclusion

In this paper, a MEMS electric field measurement sensor model based on the piezoelectric-piezoresistive coupling is constructed by the finite element method, and the steady-state characteristics of the micro electric field sensor under different sizes of piezoelectric materials and semiconductor membranes are simulated and analyzed, and the following conclusions are obtained:

As the side length of the piezoelectric material increases, the difference in peak displacement between different side lengths of the piezoelectric material is small, but the difference in the amount of strain is large. The strain component and the amount of displacement increase from the center of the membrane, and reach the peak value near the piezoelectric material boundary.

As the thickness of the piezoelectric material increases, the piezoelectric effect is more obvious, and the overall strain amount increases, but the distance between the cavities becomes shorter and the strain peak decreases. Therefore, both the strain amount and the maximum deformation displacement on the semiconductor membrane show a downward trend; the average strain amount first increases and then tends to be stable, and the displacement amount first increases and then decreases slowly.

As the thickness of the semiconductor membrane increases, its strain sensitivity decreases. The maximum strain on the membrane first increases slowly and then decreases, the average value is in a slow increasing trend, and the displacements all show a decreasing trend.

The piezoelectric material with side length $d_1 = 400 \mu\text{m}$, thickness $h_1 = 350 \mu\text{m}$, semiconductor membrane thickness $h_2 = 20 \mu\text{m}$, semiconductor side length $d_2 = 500 \mu\text{m}$ has high sensitivity, and meets the design requirements for electric field measurement.

By studying the strain on the surface of the membrane, the optimal doping area for placing the varistor patch was designed. Tests the output characteristics of the

sensor in a uniform electric field of $0\text{--}2.86 \times 10^{-6} \text{ V/m}$, thus verifying the feasibility of the sensor in electric field measurement.

Data availability statement

The original contributions presented in the study are included in the article/Supplementary Material, further inquiries can be directed to the corresponding author.

Author contributions

GL guided the experimental simulation. YY is responsible for writing the paper. Other provided some guidance.

Conflict of interest

BL was employed by China Southern Power Grid Technology Research Institute Co., Ltd. YG was employed by China Southern Power Grid Co. Ltd EHV Transmission Company Guangzhou Bureau. SC was employed by Guangdong Shuangdian Technology Co., Ltd

The remaining authors declare that the research was conducted in the absence of any commercial or financial relationships that could be construed as a potential conflict of interest.

Publisher's note

All claims expressed in this article are solely those of the authors and do not necessarily represent those of their affiliated organizations, or those of the publisher, the editors and the reviewers. Any product that may be evaluated in this article, or claim that may be made by its manufacturer, is not guaranteed or endorsed by the publisher.

References

- Ando, B., Baglio, S., Savalli, N., and Trigona, C. (2011). Cascaded "triple-bent-beam" MEMS sensor for contactless temperature measurements in nonaccessible environments. *IEEE Trans. Instrum. Meas.* 60 (4), 1348–1357. doi:10.1109/tim.2010.2101310
- Aristizabal-Tique, V. H., Gómez-Montoya, N. A., Salazar-Escobar, H., Velez-Hoyos, F. J., and Florez-Velasquez, C. A. (2020). Performance parameters estimation of Pockels high-voltage sensors by means of numerical optimization. *IEEE Trans. Instrum. Meas.* 69 (4), 1540–1546. doi:10.1109/tim.2019.2912590
- Chen, W., Li, B., and Huang, J. (2016). A CMOS MEMS humidity sensor enhanced by a capacitive coupling structure. *Micromachines* 7 (5), 74. doi:10.3390/mi7050074
- Cui, Y., Yuan, H., Song, X., Zhao, L., Liu, Y., and Lin, L. (2017). Model, design, and testing of field mill sensors for measuring electric fields under high-voltage direct-current power lines. *IEEE Trans. Ind. Electron.* 65 (1), 608–615. doi:10.1109/tie.2017.2719618
- Frantlovic, M., Jokic, I., Lazic, Z., Smiljanic, M., Obradov, M., Vukelic, B., et al. (2016). A method enabling simultaneous pressure and temperature measurement using a single piezoresistive MEMS pressure sensor. *Meas. Sci. Technol.* 27 (12), 125101. doi:10.1088/0957-0233/27/12/125101
- Iqbal, F., and Lee, B. (2018). "Measurement uncertainties in electrostatic actuated MEMS resonators[C]," in Symposium on Design, Test, Integration & Packaging of MEMS and MOEMS, Italy, May 22–May 25, 2018.

- Kainz, A., Steiner, H., Schalko, J., Jachimowicz, A., Kohl, F., Stifter, M., et al. (2018). Distortion-free measurement of electric field strength with a MEMS sensor. *Nat. Electron.* 1 (1), 68–73. doi:10.1038/s41928-017-0009-5
- Liu, L., Li, X., Wen, T., Zhang, R., Wu, Z., Zhao, J., et al. (2019). Investigation on surface electric field distribution features related to insulator flashover in SF₆ gas. *IEEE Trans. Dielectr. Electr. Insul.* 26 (5), 1588–1595. doi:10.1109/tdel.2019.008194
- Liu, L., Li, X., Zhang, Q., Liang, C., Ren, H., Zhao, J., et al. (2018). The influence of electric field distribution on insulator surface flashover[C],” in IEEE Conference on Electrical Insulation and Dielectric Phenomena, Cancun, Mexico, October 21–October 24, 2018
- Nag, M., Singh, J., Kumar, A., and Singh, K. (2020). A high sensitive graphene piezoresistive MEMS pressure sensor by integration of rod beams in silicon diaphragm for low pressure measurement application. *Microsyst. Technol.* 26 (9), 2971–2976. doi:10.1007/s00542-020-04890-x
- Qi, B., Zhao, X., and Li, C. (2016). Methods to reduce errors for DC electric field measurement in oil-pressboard insulation based on Kerr-effect. *IEEE Trans. Dielectr. Electr. Insul.* 23 (3), 1675–1682. doi:10.1109/tdel.2016.005507
- Sahay, R., and Jindal, S. K. (2021). Design and analysis of a MEMS pressure sensor with a bossed membrane and ancillary bi-functional frog arm structure for low pressure measurement. *J. Comput. Electron.* 20 (2), 1012–1019. doi:10.1007/s10825-021-01660-4
- Shanhong, X., Hucheng, L., Jun, Liu., Chu, et al. (2021). Research and development on MEMS based electric field sensor[C]//International conference on solid-state sensors. *Actuators Microsystems* 12 (7).
- Torunbalci, M. M., Alper, S. E., and Akin, T. (2015). “The advanced MEMS process for fabricating wafer level vacuum packaged SOI-MEMS devices with embedded vertical feedthroughs[C],” in 2015 Transducers – 2015 18th International Conference on Solid-State Sensors, Actuators and, Alaska, USA, June 21–June 25, 2015.
- Wang, J., Wu, H., Deng, Z., Peng, Z., and Liao, J. (2015). E-field distribution analysis on three types of converter double valve in 800kV valve hall[C],” in 2015 IEEE 11th International Conference on the Properties and applications of Dielectric Materials, Australia, July 19–July 22, 2015
- Wu, H., Li, C., Qi, B., Zhao, X., Li, J., and Zhao, L. (2012). The electric field distribution in oil-paper insulation under combined AC-DC voltage[C],” in 2012 IEEE International Conference on Condition Monitoring and Diagnosis, Bali, Indonesia, September 23–September 27, 2012
- Yang, Q., Sun, S., Han, R., Sima, W., and Liu, T. (2015). Intense transient electric field sensor based on the electro-optic effect of LiNbO₃. *AIP Adv.* 5 (10), 107130. doi:10.1063/1.4934720
- Yong, C., Haiwen, Y., Xiao, S., Luxing, Z., Yumeng, L., and Liwei, L. (2018). Model, design, and testing of field mill sensors for measuring electric fields under high-voltage direct-current power lines[J]. *Industrial Electron. IEEE Trans.* 65 (1), 608.
- Zeng, R., Zhuang, C., Niu, B., Yu, Z., and He, J. (2013). Measurement of transient electric fields in air gap discharge with an integrated electro-optic sensor. *IEEE Trans. Plasma Sci. IEEE Nucl. Plasma Sci. Soc.* 41 (4), 955–960. doi:10.1109/tps.2013.2249669
- Zhang, J., Lu, T., Zhang, W., Zhang, X., and Hu, Y. (2019). Calculation of RFI from valve hall in MMC-HVDC converter station. *Int. J. Appl. Electromagn. Mech.* 59 (1), 27–37. doi:10.3233/jae-171230
- Zhao, D., Wang, Y., Shao, J., Zhang, P., Chen, Y., Fu, Z., et al. (2021). Temperature and humidity sensor based on MEMS technology. *AIP Adv.* 11 (8), 085126. doi:10.1063/5.0053342